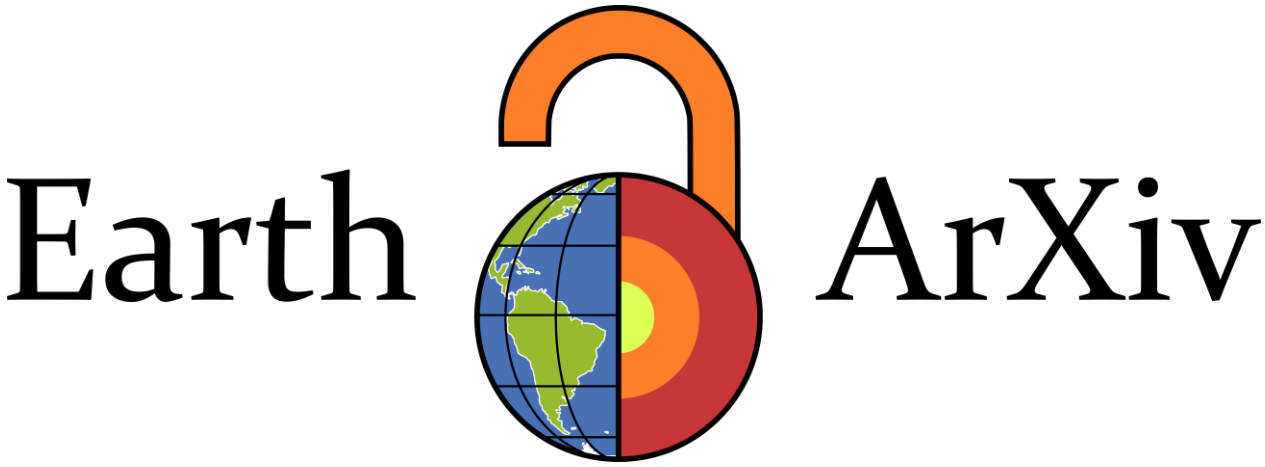

Biomineralisation for Sustainable Ecotoxic Metal Immobilisation via Enzyme Induced Carbonate Precipitation

Dickinson, Heloisa[a]; MacDonald, John[a]; Toney, Jaime L.[a]
[a]School of Geographical and Earth Sciences, University of Glasgow

Abstract

Heavy metal contamination of water presents a critical global challenge driven by the persistence and toxicity of elements such as arsenic, cadmium and lead. Conventional remediation strategies, such as Enzyme-Induced Carbonate Precipitation (EICP), typically rely on commercial urease and a multi-step extraction process, which increases energy demand, generates ammonium byproducts, and requires significant chemical inputs. In this study, we introduce a streamlined EICP approach employing crude soybean urease extract to treat a range of nine ecotoxic metals (As, Cd, Co, Cr, Cu, Li, Ni, Pb, Zn) in aqueous solutions. Crystallographic and morphological analyses revealed calcite as a recurring phase across all treatments, with element-specific carbonate minerals, such as otavite and cerussite, detected in the corresponding systems. The method integrates low-power juicing, single-step filtration, and minimal reagent use, delivering effective removal, while only arsenic and copper exhibited notable enzymatic inhibition. Compared with conventional protocols, the proposed adaptive optimisation workflow lowered energy demand, reduced chemical inputs, and mitigated greenhouse gas emissions. By incorporating waste-derived calcium and urea, the process establishes a closed-loop cycle, offering pathways for application in engineered treatment plants, active dosing systems, or passive remediation schemes. Future work should focus on mixed-metal systems and molecular-scale mechanisms to strengthen the foundation for the field-scale deployment of this sustainable strategy.

1. Introduction

Ecotoxic metal (EM) contamination in soil and water is among the most critical environmental challenges of the 21st century (UNEP, 2021). Anthropogenic activities such as industrial processes, vehicle emissions, and agricultural runoff have led to the widespread release of ecotoxic metals into terrestrial and aquatic environments. Due to their non-biodegradable nature, these contaminants persist for decades in soils and water bodies, posing environmental and public health risks, including ecosystem degradation, biodiversity loss, and human exposure through direct contact, ingestion, or contaminated food and water. In urban areas, where most of the global population is concentrated and continues to grow, climate change and the urban heat island effect combine with existing pollution to intensify thermal stress, alter hydrological cycles, and increase the mobility and bioavailability of contaminants [Wu et al., 2024, Shi et al., 2012].

Given the widespread and persistent nature of urban pollution, various soil and water remediation strategies have been developed in recent decades, including chemical, physical, and biological methods. However, many conventional approaches face challenges related to cost, scalability, or environmental compatibility. As a result, biomineralisation-based techniques have gained attention for their ability to generate stable mineral phases that immobilise ecotoxic metals. One such method, enzyme-induced carbonate precipitation (EICP), employs urease extracted from non-microbial sources, typically plants like soybean and sword bean. By catalysing urea hydrolysis, urease produces ammonia and carbonate ions that drive calcium carbonate formation, offering a biosafe and controllable alternative to microbially induced carbonate precipitation (MICP) (Saif et al., 2022; Rajasekar et al., 2025; Bian et al., 2024). A concurrent by-product of this reaction is ammonium (NH_4^+), which may pose environmental concerns if not managed appropriately, representing an important consideration for large-scale implementation (Saif et al., 2022; Rajasekar, 2025).

The alkalinity generated during EICP reactions further enhances carbonate ion concentrations, favouring $CaCO_3$ precipitation while simultaneously lowering metal solubility. Metals may then be immobilised through discrete carbonate phases (e.g., cerussite, smithsonite) (Li et al, 2022; Wang et al., 2022), solid-solution substitution within calcite/aragonite lattices (Wang et al., 2023; Zeng et al., 2025), or by co-precipitation and adsorption processes (Bian et al., 2024; Wang et al., 2023).

Biomolecules present in crude urease extracts, such as proteins, amino acids, and polysaccharides, have been shown to modulate mineral nucleation, influence crystal morphology, and enhance the stability of both crystalline and amorphous metal-bearing phases (Chen et al, 2024, 2025, Orme et al., 2001). These crude soybean urease extracts contain amino acids, proteins, and polysaccharides that expose functional groups (e.g., carboxyl, amine, and phenolic). These organic molecules can bind Ca^{2+} ions, act as heterogeneous nucleation sites, and adsorb onto crystal planes, thereby influencing the morphology, growth, and distribution of $CaCO_3$ during EICP (Shu et al., 2022; Chen et al., 2025).

Several studies have demonstrated the potential of enzyme-induced carbonate precipitation (EICP) for aqueous-phase ecotoxic metal remediation. These works have focused on different aspects of the technique, ranging from optimising calcium sources and urease activity to elucidating crystallisation pathways and assessing long-term stability in selected metal systems. Abdel-Gawwad et al. (2020) showed efficient removal of Pb^{2+}, Cu^{2+} and Ni^{2+}, with lead almost completely immobilised as nano-carbonates within hours. Wang et al. (2022) examined how urease concentration and calcium source influence Pb^{2+} removal, reporting near-complete immobilisation and proposing a precipitation sequence from $PbCl_2$ to $PbCO_3$ and $CaCO_3$. Li et al. (2022) focused on Cd^{2+}, demonstrating concurrent mechanisms of nucleation, chemisorption and co-precipitation, with crystalline otavite identified as the dominant product in systems with carbonate precipitation of Mg^{2+}/Ca^{2+}. Bian et al. (2024) highlighted that moderate Ca^{2+} concentrations enhanced the immobilisation of Zn^{2+} and Ni^{2+}, whereas excess Ca^{2+} suppressed urease activity, and further noted that organic molecules may stabilise

poorly crystalline carbonate phases. Most recently, Zeng et al. (2025) utilised soybean-derived urease to generate porous vaterite capable of selectively adsorbing Cu^{2+}, Pb^{2+} and Cd^{2+}, achieving exceptionally high sorption capacities and maintaining over 80% efficiency for Cd^{2+} after several weeks. Collectively, these findings demonstrate that metal retention via EICP is predominantly governed by pH, calcium availability and species, and the biochemical composition of the urease extracts. To provide a consolidated overview of the recent progress in this area, Table 1 summarises the key conditions and outcomes reported in studies employing EICP for the removal of ecotoxic metals from aqueous solutions. The table highlights differences in target metals, reagent concentrations, urease sources and activities, removal efficiencies, and the mineral phases identified. This synthesis underscores both the versatility of EICP and the variability of outcomes depending on system-specific factors.

The mineralogical properties of carbonate phases formed during EICP play a key role in determining both the long-term stability of immobilised metals and the potential for carbon storage. Calcite, the thermodynamically stable polymorph of calcium carbonate, is more resistant to dissolution and transformation than metastable forms such as vaterite or amorphous carbonates (Morse et al., 2007). Its formation not only supports durable metal retention (Chen et al., 2024) but also enables the incorporation of atmospheric or waste-derived CO_2, providing dual environmental benefits (Bian et al., 2025; Zhao et al., 2024).

This is the first study to systematically assess EICP performance across a wide range of ecotoxic metals under controlled aqueous conditions. In addition, we propose the concept of adaptive optimisation, a feedback-driven strategy that streamlines crude urease workflows, reduces chemical inputs, and aligns with circular economy principles. Together, these contributions lay the groundwork for scalable and sustainable deployment of EICP-based remediation strategies. In this paper, we evaluated the performance of EICP in immobilising As, Cd, Co, Cr, Cu, Li, Ni, Pb, and Zn, at concentrations of 2, 5, and 20 millimolar in aqueous systems. Four key parameters were assessed: final pH, precipitate mass, ammonium production, and metal removal efficiency. In addition, mineralogical characterisation of the solid products was conducted using scanning electron microscopy and X-ray diffraction with Rietveld refinement to identify and quantify the crystalline phases.

Table 1. Summary of recent studies employing or revising EICP for the removal of ecotoxic metals from aqueous solutions. Conditions include metal concentration, urea and calcium chloride dosages, urease source and activity, removal efficiency, and mineral phases identified via XRD or other characterisation methods. Urease activity is reported either as enzymatic units (U/g or U/mL) or as urea hydrolysis rate (mM urea min^{-1}) depending on the method used (EC: electrical conductivity; Nessler's; indophenol blue).

Study	Metal(s)	Metal conc.	Urea (M)	$CaCl_2$ (M)	Urease source	Urease activity	Removal Efficiency	Phases Identified
Xu et al. (2025)	Cd^{2+}, Pb^{2+}, Cu^{2+}	1.5–1.7 mM (per metal; mg L^{-1} varies by metal)	0.25–1.0	0.25–1.0	Defatted soybean meal, cold extract, crude	0.5–2.0 U/mL (indophenol blue method)	Cd^{2+}: 98.7% Pb^{2+}: 99.1% Cu^{2+}: 95.3%	Cerussite ($PbCO_3$) Otavite ($CdCO_3$) Malachite ($Cu_2(OH)_2CO_3$) Amorphous $CaCO_3$ observed in all treatments
Zeng et al. (2025)*	Cd^{2+}, Pb^{2+}, Cu^{2+}	200 mg L^{-1} (single-metal); 100 mg L^{-1} each (multi-metal)	0.2–1.6 (1:1 with Ca^{2+}; 0.8 optimum for vaterite synthesis)	0.2–1.6 (0.8 optimum)	Soybean-derived crude urease	18 U (diluted to 9 U for synthesis), Nessler method	Individual systems: ~88–97% removal within days; Langmuir q_m: Cu^{2+} 1207 mg g^{-1} > Cd^{2+} 786 mg g^{-1} > Pb^{2+} 655 mg g^{-1}; multi-metal shows competition	Sorbent: vaterite ($CaCO_3$) → partial calcite over time; Products: $CdCO_3$, $PbCO_3$ / $Pb_3(CO_3)_2(OH)_2$; Cu^{2+}: $Cu_2Cl(OH)_3$ (in Cl^- media)
Chen et al. (2024)	Zn^{2+}	10mM	0.5	0.5	*Canavalia ensiformis* (jack bean) and *C. gladiata* (sword bean)	1.0 g/L de extrato bruto (no mention of urease activity)	Zn^{2+}: 98.1–99.4%	$ZnCO_3$, $Zn(OH)_2$, $Zn_5(CO_3)_2(OH)_6$
Bian et al. (2024)	Zn^{2+}, Ni^{2+}	≈3.06 mM Zn^{2+} ≈3.41 mM Ni^{2+}	0.75	0, 0.25, 0.5	*Canavalia gladiata* (sword bean), crude extract	~15 mM urea min^{-1} (ammonium-rate method, at 25 g L^{-1} extract)	Zn^{2+}: 98.7% Ni^{2+}: 62.4%	$ZnCO_3$, $Zn(OH)_2$, $Zn_5(CO_3)_2(OH)_6$, $NiCO_3$
Wang et al. (2023)	Pb^{2+}, Cu^{2+}	5–50mM	0.5	0.25	*Canavalia ensiformis* (jack bean) crude, ethanol-extracted	342.7 U·g^{-1} (Nessler); ≈5.06 mM urea·min^{-1} (Whiffin method)	≈100% across 5–50 mM	Biotic: cerussite $PbCO_3$, phosgenite $Pb_2Cl_2CO_3$ (when CO_3^{2-} limited); Abiotic: cotunnite $PbCl_2$, Pb(OH)Cl
Li et al. (2022)	Cd^{2+}	5.46 mM	0.333	Ca/Mg supplied as acetates; five Mg:Ca sets	*Canavalia ensiformis* (jack bean)	5 U/mL Nessler's color reagent (NCR) assay	≥99.9% Cd	Otavite ($CdCO_3$); calcite ($CaCO_3$) with Cd co-precipitation; vaterite/aragonite

				(mM:mM): 10:10, 20:10, 30:10, 20:20, 20:6.7				($CaMg(CO_3)_2$) with chemisorption; dolomite present
Wang et al. (2022)	Pb^{2+}	5, 10, 30, 40, 50 mM	0.5	0.25	*Canavalia ensiformis* (jack bean), crude extract	342.7 U/g (Nessler's reagent colorimetric) or 99.8 mM urea min^{-1} (EC)	> 99.5% for all treatments	Biotic: cerussite $PbCO_3$, hydrocerussite $Pb_3(CO_3)_2(OH)_2$, calcium carbonate $CaCO_3$ Abiotic: cotunnite $PbCl_2$, lead hydroxide $Pb(OH)_2$, calcium hydroxide $Ca(OH)_2$
Abdel-Gawwad et al. (2020)	Pb^{2+}, Cu^{2+}, Ni^{2+}	50–200 mM	0,05–0,20	No source of Ca	*Canavalia ensiformis* (jack bean) crude	1 mg of PDUE hydrolyzes ~3 mg of urea	Pb ≈99–100% Cu ≈67–68%; Ni ≈58%	Cerussite ($PbCO_3$, 4–15 nm); malachite hexahydrate ($CuCO_3 \cdot Cu(OH)_2 \cdot 6H_2O$, ~8 nm–thick sheets); hellyerite ($NiCO_3 \cdot 6H_2O$, ~0.30 µm–thick sheets)
Rajasekar et al. (2025	Rajasekar et al. (2025) conducted a non-experimental comparative review of MICP and EICP for heavy-metal remediation, synthesising mechanisms, operational conditions (pH/temperature/urease sources), reported efficiencies and typical carbonate phases, and discussing the advantages and limitations of each approach.							

* EICP used to synthesize vaterite; metal removal assessed by adsorption with pre-formed $CaCO_3$, not in situ EICP precipitation.

1.1. Theoretical Framework: EICP and Ecotoxic Metal Immobilization

Enzyme-Induced Carbonate Precipitation (EICP) is a bio-mediated strategy for the immobilisation of heavy metals in contaminated matrices. It relies on the urease-catalysed hydrolysis of urea, generating ammonium and carbonate ions according to the reaction (Nemati & Voordouw, 2003):

$$CO(NH_2)_2 + H_2O \xrightarrow{\text{urease}} 2NH_3 + CO_2 \qquad (\textit{Equation 1})$$

This is followed by the conversion of CO_2 in water to carbonate ions under alkaline conditions. The overall process increases pH and promotes supersaturation with respect to calcium carbonate, enabling mineral precipitation (Ahenkorah et al., 2021):

$$Ca^{2+} + CO_3^{2-} \rightarrow CaCO_3\downarrow \qquad (\textit{Equation 2})$$

These precipitates function both as structural scaffolds and as active phases that sequester metal ions through inorganic and organic pathways. Inorganic immobilisation involves multiple mineralogical mechanisms: co-precipitation with $CaCO_3$ via surface adsorption, isomorphic substitution (e.g. Cd^{2+}, Zn^{2+} partially replacing Ca^{2+} in the calcite lattice forming solid solutions), occlusion within growing crystals, or mechanical entrapment among crystal aggregates (Kim et al., 2023; Xu et al., 2025). These substitution processes can be expressed by the general solid-solution reaction:

$$CaCO_3(s) + x\,M^{2+} \rightleftharpoons Ca_{1-x}M_xCO_3(s) + x\,Ca^{2+}\ (\text{solid solution}) \qquad (\textit{Equation 3})$$

In the context of EICP, thermodynamic modelling and experimental studies confirm that metals such as Ni^{2+}, Cd^{2+}, and Pb^{2+} can be incorporated into calcite lattices through surface and subsurface substitution (Xu et al., 2025). When the solubility product of a given metal carbonate is sufficiently low, discrete phases such as cerussite ($PbCO_3$), smithsonite ($ZnCO_3$), or otavite ($CdCO_3$) may form independently under ureolytic conditions, further enhancing immobilisation efficiency (Achal & Pan, 2014):

$$M^{2+} + CO_3^{2-} \rightarrow MCO_3\ (\text{solid}) \qquad (\textit{Equation 4})$$

$$M^{2+} + CO_3^{2-} + nH_2O \rightarrow MCO_3{\cdot}nH_2O\ (\text{solid}) \qquad (\textit{Equation 5})$$

Metals that do not enter the calcite lattice can still be immobilised by encapsulation within porous $CaCO_3$ matrices (Xu et al., 2025). Moreover, the rise in pH during ureolysis facilitates the formation of metal hydroxides (e.g., $Cr(OH)_3$, $Fe(OH)_3$, $Zn(OH)_2$), further reducing solubility (Achal & Pan, 2014; Bian et al., 2024). In phosphate-

rich systems, highly insoluble phases such as $Pb_3(PO_4)_2$ or pyromorphite may form, enhancing selectivity and permanence (Li et al., 2021; Ryan et al., 2001).

Organic-mediated immobilisation in EICP arises from interactions between metals and biomolecules in crude plant-derived urease extracts (e.g., soybean or sword-bean). Functional groups (–SH, –COOH, $–NH_2$) drive complexation, chelation, and sorption on organic matrices, while ligand exchange stabilises ions at proteinaceous or polysaccharide surfaces (Shu et al., 2022; Baffoe & Ghahremaninezhad, 2022; Chen et al., 2024). Biomolecules can also template $CaCO_3$ nucleation, altering morphology, phase stability, and crystallinity, with some ligands becoming occluded during growth (Addadi & Weiner, 1985; Baffoe & Ghahremaninezhad, 2022). Redox-active compounds (e.g., phenolics) may further reduce Cr^{6+} to Cr^{3+}, enhancing immobilisation (Dickinson et al., 2025). Collectively, these processes form a dynamic continuum of biomolecule-driven crystallogenesis spanning nucleation, growth modulation, and post-crystallisation reactions that shapes mineral reactivity and long-term stability (Weiner & Addadi, 2011; Chen et al., 2024).

2. Experimental Section

2.1. Materials

Mineral precipitation in aqueous solutions containing nine different ecotoxic metals (EMs) - As, Cd, Co, Cr, Cu, Li, Ni, Pb, and Zn - was studied at 2 mM, 5 mM, and 20 mM. The experiment utilized a crude urease extract derived from soybeans (*Glycine max*), a 1 M solution of urea, and calcium chloride ($CaCl_2$) as the calcium source. The soybeans were sourced from the Jalpur brand and purchased in a local supermarket, while the urea (98% purity) and metal salts ($CdCl_2$, $CoCl_2$, $Cr_2(SO_4)_3{\cdot}xH_2O$, $CuCl_2$, $AsCl_3$, LiCl, $NiCl_2$, $PbCl_2$, and $ZnCl_2$) were obtained from Sigma-Aldrich. All metal salts used were anhydrous and had a purity level of ≥99.995%. For solution preparation, deionized water with a resistivity of 18.2 MΩ·cm, provided by the Milli-Q ultrapure system in the University of Glasgow's Environmental Biogeochemistry laboratory, was employed. Full technical specifications and operational details for all equipment and methodologies used in this study are provided in the Supplementary Information.

2.1.1. Crude Urease Extract Preparation

To prepare the crude urease extract (CUE), 80 grams of whole soybeans were soaked in deionised water and blended to a total final volume of 1 L. After standing overnight at room temperature, the solution containing soybeans was processed using a Fridja f1900 masticating juicer (1 L capacity, 250 W) to separate solids from the liquid extract. To facilitate protein precipitation, calcium carbonate ($CaCO_3$) was added to the extract, reaching an approximate concentration of 0.06 M. The mixture was allowed to settle for two hours, after which the supernatant was carefully decanted. This supernatant was then centrifuged at 3700 rpm for 15 minutes at 4°C and filtered through

standard laboratory-grade filter paper (Grade 2) to obtain a clarified enzyme solution. Urease activity was assessed following the method established by Whiffin (2004), with an average activity of 2.66 ± 0.7 mM urea·min^{-1}.

2.1.2. Preliminary Optimization of Soybean Concentration and Operational Parameters

The soybean extract concentration and operational parameters were optimized to determine the lowest soybean concentration that would achieve maximum calcium precipitation without excessive ammonium production. A series of tests were conducted, varying soybean extract concentrations (20, 40, 60, 80, and 100 g/L) and urea concentrations (0.25, 0.5, 0.75, and 1.0 M) to identify the ideal urease activity. The objective was to achieve sufficient urease activity to precipitate all the calcium in the precipitation solution without overproducing ammonium. This optimization led to an optimal soybean extract concentration of 80 g/L, corresponding to urease activity in the range of 2.66 mM urea·min^{-1}. This level of urease activity was sufficient to fully precipitate all the calcium from the 1 M $CaCl_2$ solution in a precipitation solution composed of 1 M $CaCl_2$, 1 M urea, and crude urease extract at a 1:1:1 ratio. This balance effectively prevented excessive ammonium production while ensuring complete precipitation. All experimental conditions were assessed in triplicate to ensure statistical reliability. Detailed information on the optimisation tests, including the method used to calculate urease activity, is provided in the Supplementary Information section.

2.2. Experimental Procedure

To evaluate metal immobilization by EICP, we prepared a solution by combining equal volumes (85 mL each) of crude urease extract, an aqueous solution of the target ecotoxic metal (2, 5 or 20 mM) and 1 M $CaCl_2$, and a solution containing 1 M of urea. This mixture was aliquoted into five 50 mL Falcon tubes, incubated at 25 °C for 72 h, and then allowed to cure at room temperature for seven days. After curing, solids were rinsed with deionized water, collected on Grade 2 filter paper, and oven-dried at 37 °C for 24 h. Subsamples of the supernatant were taken for pH, conductivity, ammonium and metal concentration analyses, and dried precipitates were stored in airtight vials for subsequent SEM, EDS and XRD characterization.

2.3. Assessment of Immobilization of EMs and Ammonium Production

The efficiency of the precipitation process in immobilizing ecotoxic metals (EMs) and ammonium was assessed by analysing the residual liquid. Solid particulates were first removed by filtering the liquid through Grade 2 filter paper (Whatman). A portion of the filtered liquid was then passed through 0.45 µm syringe filters for ammonium determination. Ammonium concentration was measured using the salicylate colorimetric method, with analysis performed on a SEAL AutoAnalyzer (AA3). pH was

recorded using a YSI ProDSS Multiparameter Probe, with recalibration conducted to ensure consistency of readings at 25 °C. For metal concentration analysis, nitric acid (HNO_3) was added to a separate aliquot of the filtered solution to achieve a final concentration of 2% (v/v). The metal content was quantified using Inductively Coupled Plasma Optical Emission Spectroscopy (ICP-OES) with a Thermo Scientific iCAP 7000.

2.4. Characterization of the Precipitates

The precipitates formed during the experiments were analysed as a single, powdery fine-grained fraction, with the size of the precipitates confirmed to be below 1 mm through visual observation. Scanning electron microscopy (SEM) was used to examine their morphology and size in detail. Powder X-ray diffraction (XRD) and Rietveld Refinement using Profex software was performed on the entire precipitate sample to identify the primary mineral phases and quantify their relative proportions for each metal and treatment condition.

2.5. Sustainability and Circular Economy

2.5.1. Adaptive optimisation aligned with waste-to-resource, circular economy and GHG protocol principles

In this work we introduce adaptive optimisation as a novel framework for biogeotechnical remediation of soils and waters, defined as a continuous, feedback-driven process designed to improve pollutant removal efficiency while reducing energy, materials, labour and other inputs. This concept, applied here for the first time, embeds circular-economy and GHG Protocol principles by ensuring that sustainability gains are realised not only in the environmental outcomes but also in the practical and economic feasibility of the workflow.

Our approach applies adaptive optimisation to transform food-processing residues into functional reagents while reducing costs, energy consumption and greenhouse-gas emissions. Instead of relying on costly commercial preparations, we extract urease from soybean by-products, thereby upcycling waste streams and lowering material expenses.

Adaptive optimisation enabled us to streamline the process, replacing resource-intensive operations with simpler steps and achieving reductions in energy use, chemical demand and processing time. These refinements resulted in measurable reductions in energy demand, processing time and chemical inputs, alongside clear cost savings. In practice, adaptive optimisation was realised by continuously testing reagent concentrations and material quantities to maintain or improve removal efficiency while simultaneously reducing inputs. A concrete example is provided by the production of crude urease extract. Whereas commonly available protocols often prescribe multiple filtration steps and the use of ethanol and acetone for urease extraction, we employed only deionised water and a single filtration step. Despite this simplification, the resulting

biomineral precipitation achieved an equivalent mass yield to that obtained through more resource-intensive methods. Although commercial $CaCl_2$ and urea were used in the present work for standardisation, both can be sourced from waste streams such as eggshells for calcium and urine for urea, thus paving the way towards fully circular EICP systems.

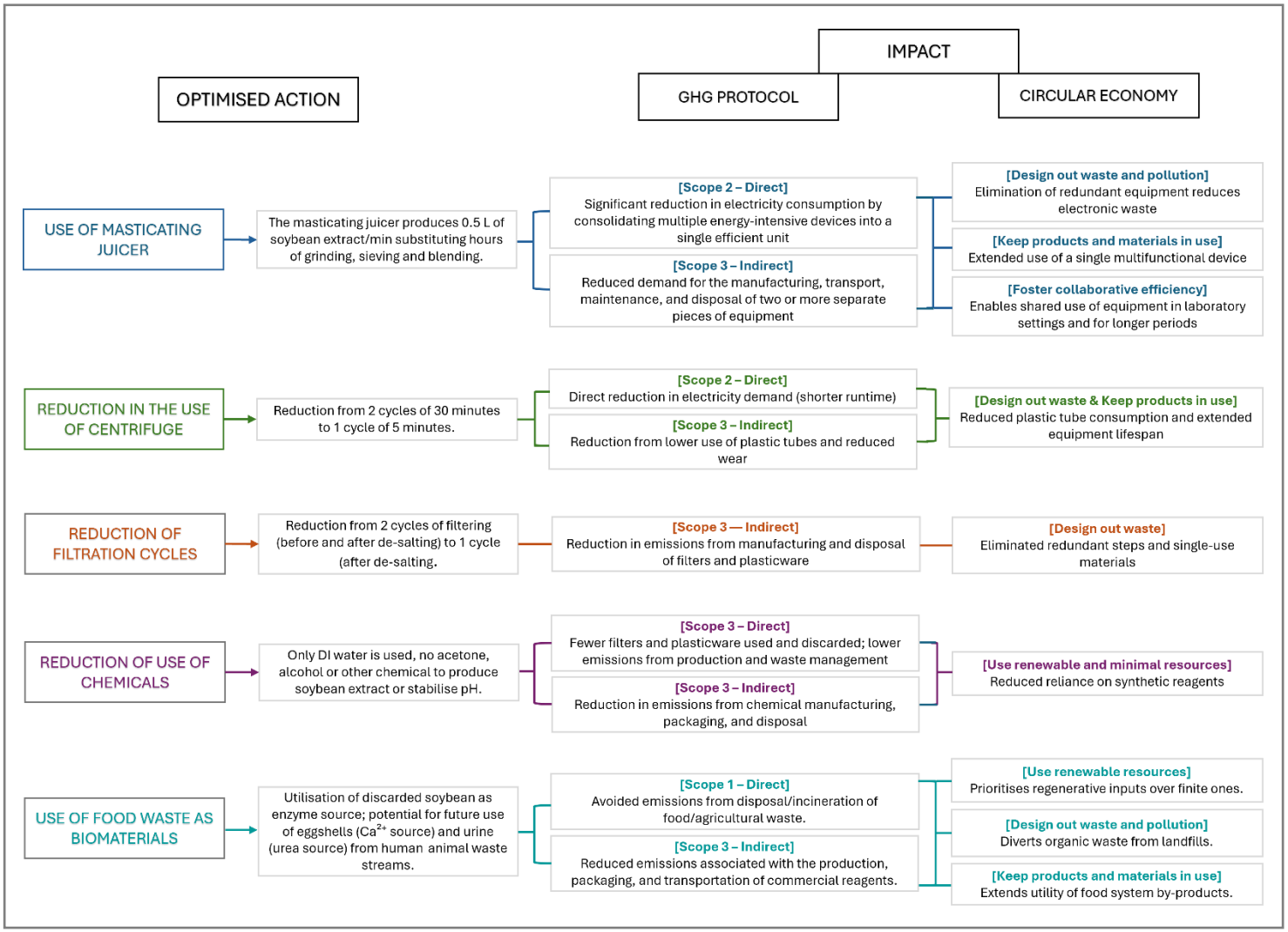

Figure 1 – Operational optimisation of crude urease extraction mapped against GHG Protocol scopes and circular economy principles. The diagram summarises key interventions introduced actions, integrating both direct and indirect emissions reductions under the GHG Protocol framework, alongside core principles of the circular economy.

3. Results

3.1. System Response Parameters

To assess system behaviour across metal treatments, we quantified four core variables: final pH, ammonium concentration, precipitate mass, and metal removal efficiency. Together, these metrics provide an integrated view of ureolysis-driven alkalisation, carbonate generation, and overall immobilisation performance. We first report pH and ammonium as direct proxies of urease activity, followed by precipitate mass and removal efficiencies. Principal carbonate morphologies were assessed by scanning electron microscopy (SEM) to characterise precipitate crystal habits and textures.

3.1.1. pH and ammonium production measurements

The final pH and residual ammonium concentrations were measured after 72 hours to evaluate ureolytic activity and system alkalisation in the presence of each metal treatment (Fig. 2). As ureolysis proceeds, the enzymatic hydrolysis of urea produces ammonium and hydroxide ions, resulting in a measurable rise in both pH and ammonium levels. Therefore, high values for both parameters are indicative of efficient urease activity, whereas reductions reflect enzymatic inhibition.

The control sample (C1), which received no metal addition, exhibited the highest final pH (8.541) and ammonium accumulation (3,852 ppm), representing unhindered ureolysis for this specific system in the absence of inhibitory effects. In contrast, metal-treated systems displayed variable reductions in both parameters, reflecting differing degrees of interference with enzymatic function and carbonate precipitation.

Among all treatments, Cu^{2+} and As^{3+} exerted the strongest inhibitory effects, as evidenced by their consistently low final pH values (6.174–6.218 for Cu; 6.666–6.913 for As) and ammonium concentrations below 1,500 ppm. These findings indicate that ureolysis was substantially suppressed in the presence of these elements at the tested concentrations.

Cr^{3+} and Cd^{2+} showed moderate reductions in ammonium production, with final pH values remaining above 8.0, indicating partial retention of urease activity. A slight downward trend in pH and ammonium across Cr^{3+} treatments (T1 to T3) was observed. By comparison, Co^{2+}, Li^{+}, Ni^{2+}, Pb^{2+} and Zn^{2+} maintained high final pH values (≥8.1) and elevated ammonium concentrations exceeding 3,300 ppm, closely approaching those of the control. These results suggest that ureolytic activity remained largely unaffected in these systems.

Overall, the data reveal a metal-specific pattern of urease inhibition, with Cu^{2+} and As^{3+} markedly impairing activity, while other metals, particularly Li^{+}, Zn^{2+} and Pb^{2+}, had minimal impact under the tested conditions.

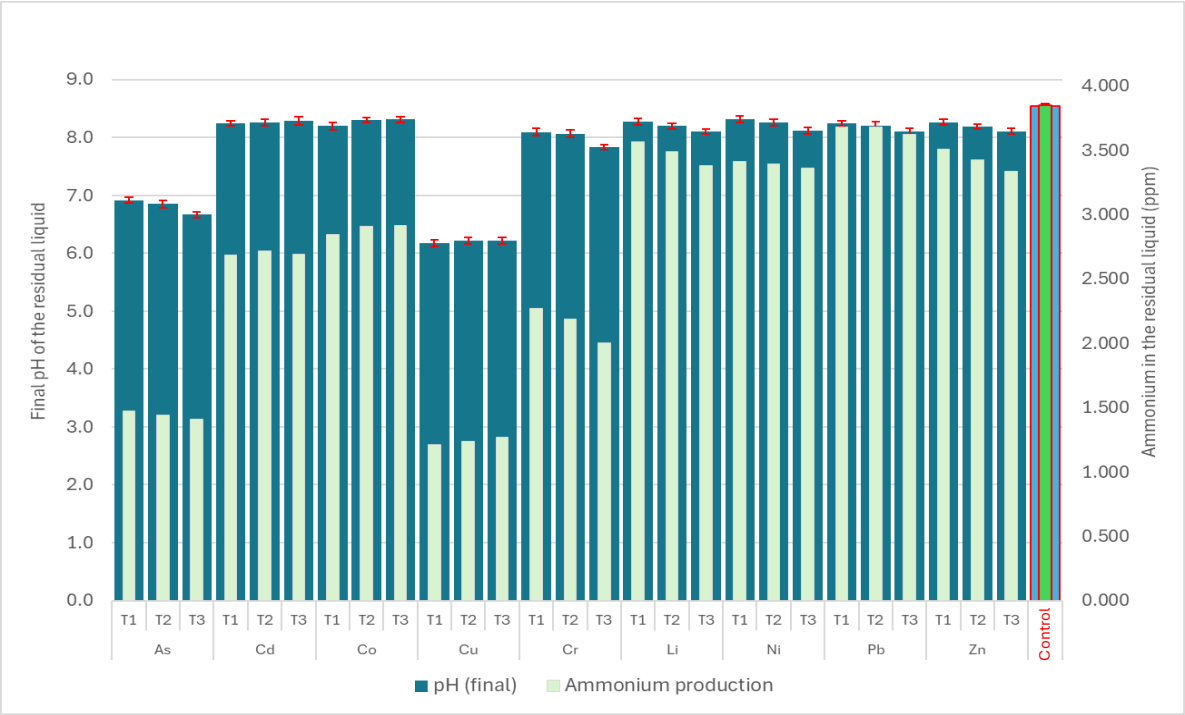

Figure 2. Final pH (blue bars) and residual ammonium concentration (green bars) measured after 72 hours of incubation in each metal treatment with N=5 for pH and N=1 for ammonium release.

3.1.2. Precipitate mass

Gravimetric analysis of the precipitates formed during the enzyme-mediated treatment process revealed distinct patterns in the mass of solids recovered per metal species across treatments T1 to T3. Figure 3 exhibits the measured values for each metal per treatment plus control.

Arsenic and copper exhibited consistently low precipitation across all treatments, with values remaining markedly below the control. Arsenic decreased from 0.431 g in T1 to 0.407 g in T3, showing a progressive but negligible reduction in mass. Copper fluctuated only slightly, increasing modestly from 0.432 g in T1 to 0.474 g in T2 before returning to 0.431 g in T3, reflecting minimal net change. Both elements showed low overall precipitation and limited responsiveness to treatment variation.

Cobalt exhibited a moderate precipitation profile with consistent values in T1 (0.750 g) and T2 (0.750 g), followed by a slight decrease to 0.583 g in T3, reflecting overall stability with a moderate reduction under the highest metal load.

Cadmium, chromium, nickel and zinc displayed higher degrees of variability. Cadmium decreased substantially from 1.801 g in T1 to 0.470 g in T3, with a sharp decline observed between T2 and T3. Chromium showed a marked reduction from 1.773 g in T1 to 0.252 g in T3, with a large drop already evident by T2. Nickel initially presented elevated mass in T1 (1.712 g), followed by a substantial decline to 0.521 in T2 and 0.409 g by T3, suggesting a pronounced downward trend. Zinc exhibited a similar pattern, with a gradual decrease from 1.757 g in T1 to 0.580 g in T3, with the most notable change occurring

between T2 and T3. These elements demonstrated high initial precipitation followed by sharp or moderate reductions, indicative of treatment-sensitive behaviour.

In contrast, lithium and lead consistently produced the highest masses among all tested elements. Lithium remained nearly constant across treatments - 1.874 g in T1, 1.875 g in T2, and 1.872 g in T3 - indicating extremely stable and elevated precipitation. Lead also exhibited minor variation, increasing slightly from 1.722 g in T1 to 1.789 g in T3. Both elements closely approached or exceeded the mass observed in the control (1.734 g for lithium and 1.806 g for lead), suggesting robust and sustained precipitation with minimal sensitivity to treatment modifications.

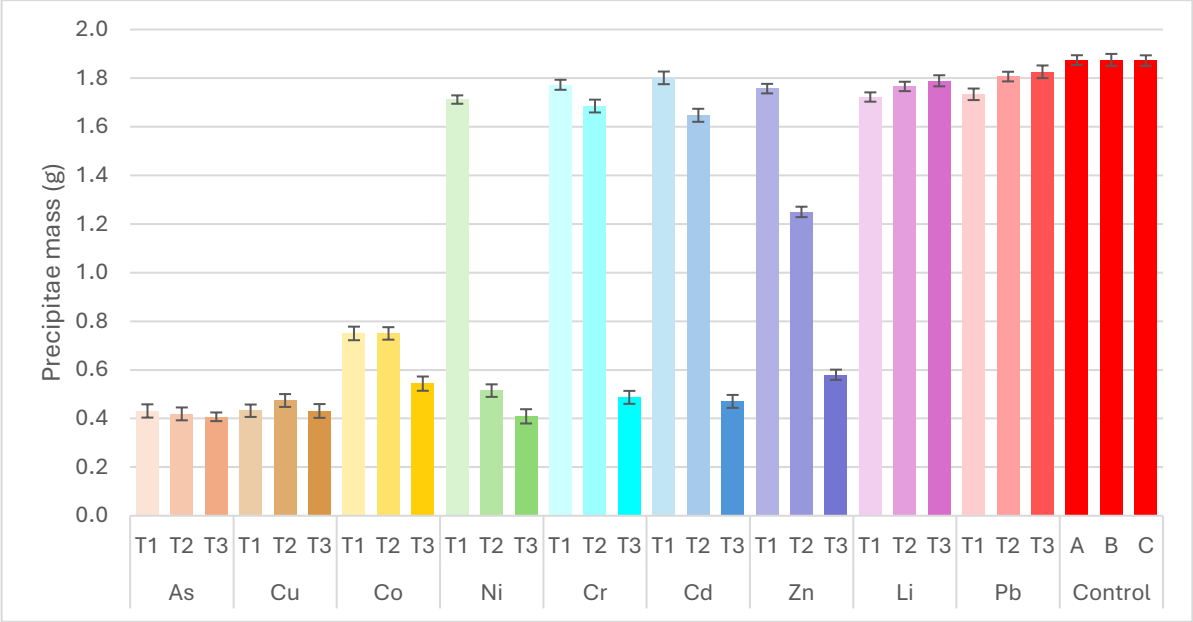

Figure 3. Mass of solid precipitate for each metal treatment (T1–T3) and control (A–C). Bars represent mean precipitate mass (g) ± standard deviation (N = 5).

3.1.3. Ecotoxic metals removal efficiency

The removal efficiencies of individual metals across treatments T1, T2, and T3 are summarised below in Fig. 4, providing a basis for comparative analysis of element-specific performance and inter-treatment variability.

Removal efficiencies across all tested metals showed consistently high values (above 70%), though distinguishable patterns emerged when grouping by performance. Based on average removal percentages across treatments T1, T2 and T3, the metals were categorised into four efficiency tiers. Lead, zinc and chromium displayed very high removal efficiencies, consistently exceeding 99% under all conditions. These were followed by cobalt and nickel, which achieved high efficiencies in the range of 95–98%, while cadmium and lithium were placed in a moderately high category, showing mean removal between 89% and 93%. Arsenic and copper, though still achieving over 70% removal, were classified as lower-efficiency elements relative to the other metals in this study.

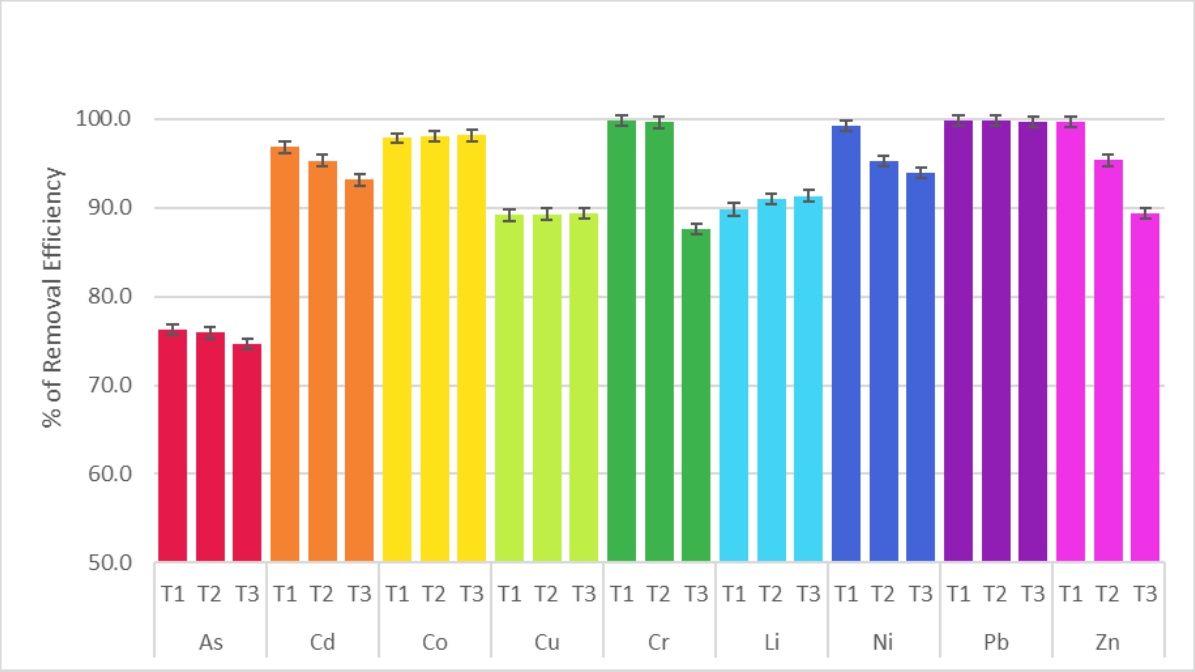

Figure 4. Metal removal efficiency (%) after 72 hours for each treatment (T1–T3) across all tested elements. Bars represent mean values ± standard deviation (N = 5).

In terms of stability across treatments, lead and zinc exhibited exceptional consistency, with deviations between T1 and T3 below 0.2 percentage points. Similarly, cobalt showed minimal fluctuation (<1%), supporting its classification as a stable element in this system. Lithium and chromium showed modest variations of approximately 1–2%, suggesting general robustness with slight sensitivity to treatment conditions. Cadmium and nickel displayed greater variation (up to 7 percentage points), indicating a possible dependency on process parameters. The highest degree of fluctuation was observed in copper, which dropped from ~79% in T1 and T2 to 69% in T3, and arsenic, which exhibited a consistent but gradually decreasing trend across treatments. These findings suggest that while removal performance was broadly high, certain metals demonstrated more sensitivity to treatment conditions than others.

3.2. Morphological and Microtextural Characterisation of Mineralogical Assemblages

All SEM micrographs were acquired at a consistent magnification, with image scales fixed at 20 µm to ensure visual comparability across treatments (Fig. 5). Carbonate precipitates in the control samples predominantly occur as spheroidal aggregates. These are observed as isolated particles, clustered groups of smaller spheres, or as paired spheroids forming composite aggregates. In many cases, spheroids are surrounded by a coarser outer overgrowth, producing a distinct core–shell texture (hereafter referred to as sunflower texture, indicated with letter S in Fig.5), where a

spheric inner core with smooth surface is enveloped by a radially crystalline crust marked by dense coverage of nanometric protrusions or microcrystalline granules, imparting a distinctly roughened appearance. Detachment of the inner sphere occasionally results in circular voids, indicating that the core and crust represent structurally distinct growth domains (Fig. 5 Control 1, 2 and 3). In addition to these features, clusters of microspheres are commonly embedded within, or coalesced into, more massive carbonate phases with relatively smooth and continuous surfaces, lacking defined substructures (indicated as M in Fig. 5 control samples). These compact morphologies contrasted sharply with the granular and radial features described above, indicating a broader diversity in precipitation habits even under control conditions.

Samples treated with Zn, Li, and Pb exhibited morphologies broadly comparable to the control, with similar combinations of spheroidal, sunflower-like, and dense granular forms (Fig. 5 Zn, Li and PB T1, T2 and T3). Minor variations were observed in crystal size and packing density across treatments. In Pb-treated samples, however, aggregates sometimes adopted a distinctive bone-like appearance, composed of interlocking, elongated structures with porous, trabecular textures (Fig. 5 Pb T1 and T3, indicated with letter B). This represented a subtle but consistent shift in crystal organisation.

Chromium-treated samples revealed a marked progression in carbonate morphologies across the experimental series. At T1, precipitates were dominated by aggregates with a distinctly crystalline habit, composed of well-developed faceted units intergrown into compact clusters and spheroids with rugged superficial microtexture. At T2, spheroidal morphologies became more abundant, often forming dense clusters and partially coating earlier crystalline fragments, indicating a shift towards rounded growth forms. By T3, the precipitates were largely composed of irregular, poorly defined aggregates with a more porous or lamellar character, lacking the sharp crystalline outlines observed at T1. This transition from faceted crystalline structures to spheroidal and ultimately less defined morphologies suggests that chromium exerts a strong control on carbonate growth pathways, progressively favouring disordered and less crystalline habits over time.

Nickel-treated samples also displayed a clear transition in carbonate morphologies through the experimental sequence. At T1, precipitates were dominated by spheroidal particles, which frequently occurred in dense clusters and in some cases fused into larger aggregates. At T2, spheroidal morphologies remained abundant, but they were increasingly associated with irregular granular overgrowths and intergrown fragments, giving rise to more heterogeneous clusters. By T3, the assemblage was characterised by the predominance of blocky to tabular aggregates, composed of equant carbonate crystals with well-developed planar surfaces and sharp edges. This progression from spheroidal to blocky morphologies indicates that, at higher concentrations, Ni appears to disfavour well-ordered crystallization, instead promoting the development of blocky aggregates with poorly defined crystalline surfaces.

Cobalt-treated samples displayed a diverse range of morphologies that shifted systematically with concentration. At low concentration (T1), carbonates formed

irregular compact aggregates with limited surface definition. Intermediate concentration (T2) promoted the appearance of spheroidal particles with striking trigonal faceted surfaces, composed of finely lamellar subunits that produced delicate filigree-like textures. At the highest concentration (T3), cobalt favoured the development of abundant spheroids, which occurred in densely packed clusters with smoother surfaces compared with the faceted forms of T2. This progression suggests that cobalt strongly influences carbonate habit, enhancing spheroidal growth while modulating the expression of faceted versus rounded surfaces.

Cadmium-treated samples showed a clear preference for faceted over spheroidal morphologies. At low concentration (T1), precipitation was dominated by sharp, blade-like and tabular crystals that intergrew into compact, highly angular aggregates. Intermediate concentration (T2) preserved this faceted habit but also introduced blocky masses with smooth, fractured surfaces, alongside occasional lamellar forms. At the highest concentration (T3), the products remained largely crystalline and faceted, with dense granular clusters replacing the spheroidal aggregates so typical of the controls. Overall, cadmium strongly favoured the development of angular, intergrown crystals and suppressed the formation of rounded spheroidal morphologies, setting it apart from most other treatments.

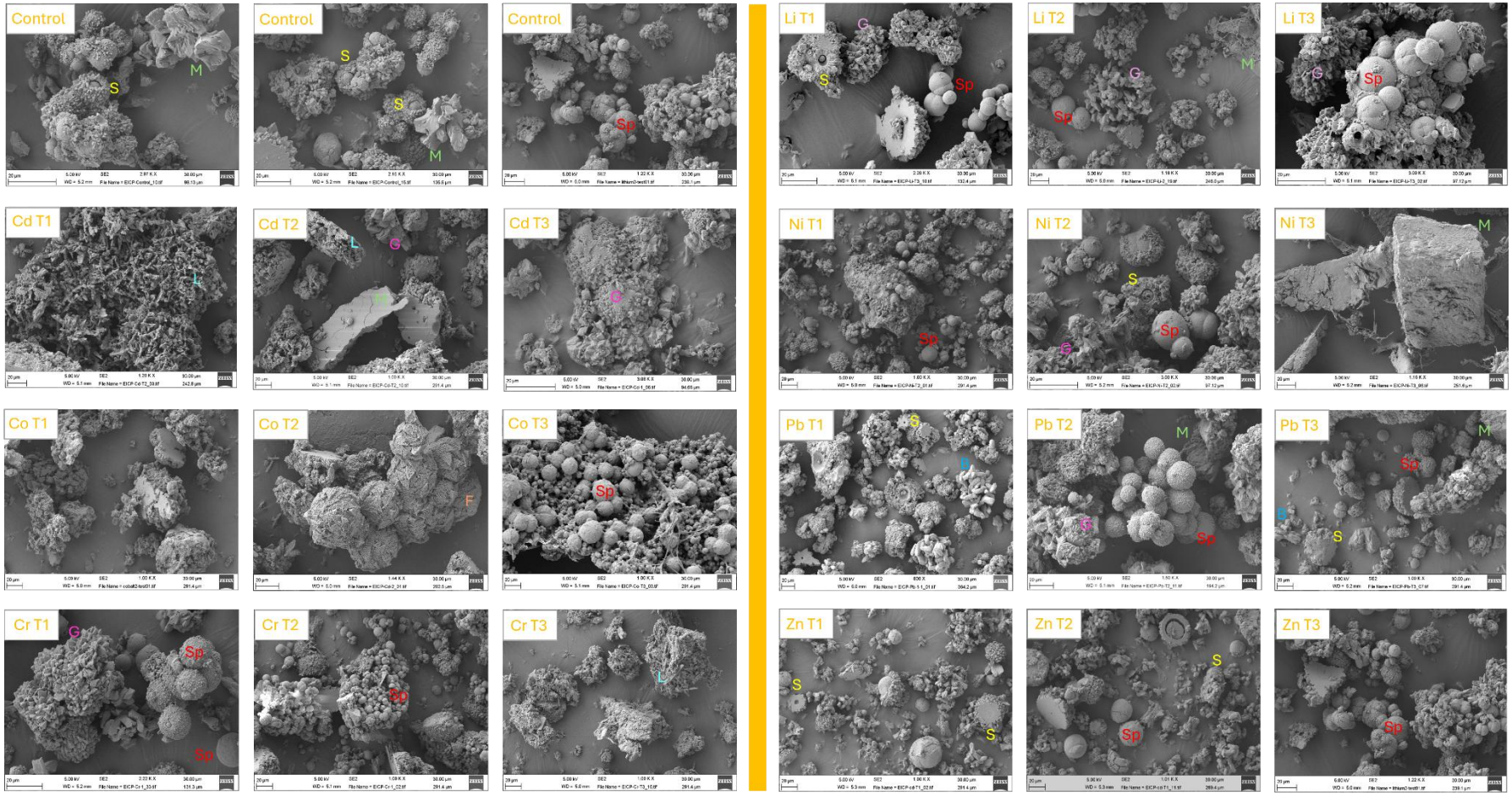

Figure 5. Scanning electron micrographs (SEMs) of precipitates recovered from the EICP experiments with nine metal ions (Co^{2+}, Cr^{3+}, Cd^{2+}, Pb^{2+}, Li^{+}, and Ni^{2+}) across three treatment levels (T1, T2, T3), alongside control conditions without metal addition, revealing substantial morphological diversity in carbonate-based precipitates. Legend of the textures present in the images: B – bone-like (blue); G - granular polyhedral (pink); L - lamellar or platey-like (acquablue) ; Sp = Spherical (red); S – sunflower-like (yellow); M = massive texture (green).

3.3. X-Ray Diffractometry and Semi-Quantitative Phase Analysis by Rietveld Refinement

The XRD patterns reveal consistent calcite formation across all treatments, with notable variations in peak sharpness and angular position, particularly around the (104) reflection (Fig. 6 A, B). Arsenic and copper treated residues were not analysed due to insufficient recovered mass for XRD preparation. In both cases, the precipitates appeared to remain impregnated within the filter paper rather than forming separable solids, suggesting the presence of poorly crystalline or potentially amorphous phases that resisted recovery.

All analysed samples exhibit calcite as the dominant crystalline phase, though differences in peak symmetry and definition are evident. Broader and less intense reflections are observed in samples treated with Ni T1 and Co T2, suggesting comparatively lower crystallinity. Variations between T1 and T2 are also apparent: in most cases, T1 treatments result in narrower peak bases than their T2 counterparts, particularly in the Co-treated samples. However, this trend is not uniform; in the Ni-treated pair, the T2 peak appears slightly sharper than that of T1, indicating the reverse pattern. In addition to calcite, Pb^{2+} formed cerussite ($PbCO_3$) in relative abundances around 2-4% (from T1 to T3), while Cd^{2+} produced trace amounts (<0.5%) of otavite ($CdCO_3$). Although refinement consistently identified cerussite in the Pb-treated samples, its diagnostic reflections are not clearly resolved in the diffractograms. This likely reflects its occurrence as a minor phase near the detection limit, overlap of its main reflections with intense calcite peaks, and possible broadening due to nanocrystalline or poorly ordered domains. Additional effects such as microabsorption in Pb-rich grains or partial Pb incorporation into calcite may further suppress discrete cerussite peaks. These reported abundances are therefore semi-quantitative, reflecting relative phase proportions from Rietveld fitting rather than absolute concentrations, and should be interpreted with caution in the absence of internal calibration standards.

The position of the (104) reflection, magnified in panel B, reveals systematic angular displacements relative to the control. The control sample itself shows a measurable shift to lower angles compared to the standard reference for pure calcite (29.40° 2θ), likely due to organic interactions during crystallisation. Among the treated samples, the Cr-treated residue exhibits the most pronounced shift, followed by Li and Ni, which display similar displacements of slightly lower magnitude. Zn, Pb and Cd treated samples show moderate shifts, while the Co-treated sample presents a peak position slightly above that of the control, indicating the smallest d-spacing among all treatments. The relative ranking of peak shift magnitude, from highest to lowest relative to the control, is: Cr > Li ≈ Ni > Zn > Pb > Cd > Control > Co. These systematic displacements likely reflect lattice distortions induced by cation substitution and, in some cases, residual organics, both of which can modify unit-cell parameters and displace the (104) reflection relative to pure calcite.

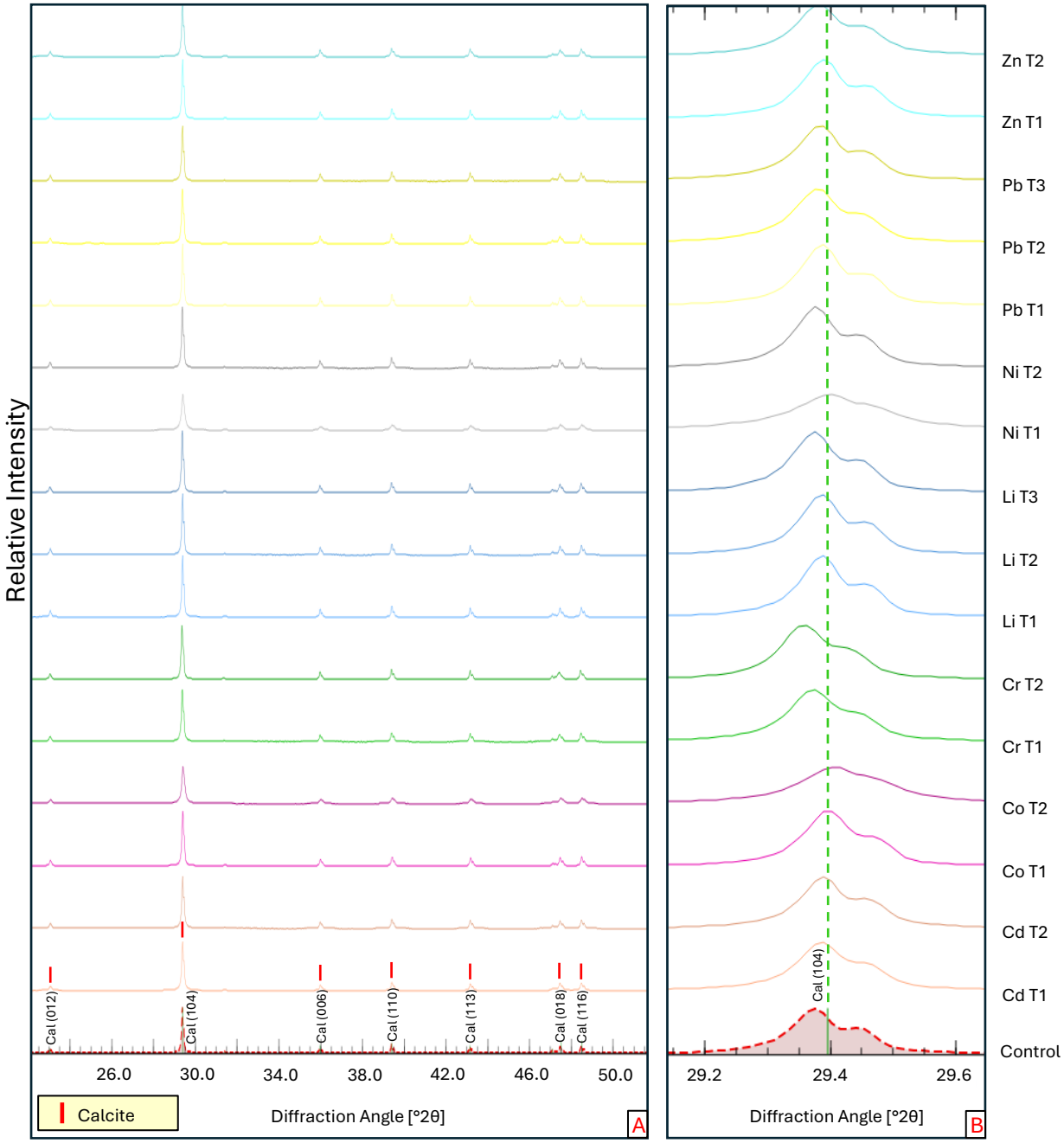

Figure 6. *(A)* Stacked X-ray diffraction (XRD) patterns of precipitates following EICP treatments with 7 of the 9 ecotoxic metals. Red markers indicate the main reflections of calcite (PDF 05-0586), confirming its predominance across all samples. *(B)* Magnified view of the calcite (104) reflection, with a green dashed line marking the standard reference position at 2θ ≈ 29.40°. The control sample is exhibited at the bottom with a red dash line.

4. Discussion

4.1 Comparative performance of metal immobilisation

efficiency of immobilisation observed in our experiments. The first group (Pb, Zn and Cr) showed the highest and most consistent retention. The second group (Ni, Co and Cd) also reached high removal, though outcomes seemed more influenced by kinetic constraints or competition with other ions. The third group (As, Cu and Li) was effectively removed as well, but with lower efficiencies and distinct mechanistic pathways compared with the divalent cations.

The first group includes elements that display strong but contrasting interactions with carbonate minerals, ranging from lattice incorporation to redox-driven precipitation. Lead can be immobilised in carbonates through three pathways: lattice substitution for Ca^{2+}, coprecipitation during calcite growth, and segregation as discrete Pb carbonates when phase separation is favoured (Reeder, 1996; Stipp et al., 1992; Zachara et al., 1991; Elzinga and Reeder, 2002). Crystallographic and spectroscopic studies show that substitution is limited but surface-mediated, occurring mainly at steps and growth fronts (Reeder and Lamble, 1999). In situ AFM and resonant X-ray reflectivity confirmed incorporation at the calcite (104) surface, with Pb displacing Ca by 0.2–0.28 Å and forming strained solid solutions (Callagon et al., 2014). In our experiments, ureolysis proceeded efficiently in the presence of Pb (final pH > 8.1; $[NH_4^+]$ > 3,300 ppm), with precipitate masses of 1.72–1.79 g and removal efficiencies consistently >99%. Calcite dominated, with only minor cerussite (2–4%) detected. XRD showed systematic (104) shifts consistent with lattice distortion (Fig. Morphologically, mineral precipitates showed sunflower-type morphology but also developed trabecular, bone-like textures, indicating Pb modulation of growth. These results suggest that Ca-driven EICP favours Pb incorporation into calcite, with limited segregation into cerussite.

The incorporation of Zn appears to be strongly structure-dependent, with calcite acting as a compatible host phase, as shown by coprecipitation and substitution studies (Kitano et al., 1973; Reeder et al., 1999). Partitioning depends on supersaturation and growth rate, with distribution coefficients decreasing slightly as growth accelerates (Mavromatis et al., 2019; Brazier et al., 2024). Mechanistically, Zn adsorbs first as tetrahedral surface complexes before dehydration allows octahedral substitution at step sites, forming dilute solid solutions with smithsonite (Elzinga and Reeder, 2002). Our experiments showed removal efficiencies of 88–99%, with pH ≥7.9 and $[NH_4^+]$ >3,300 ppm. Precipitate masses declined from 1.757 g in T1 to 0.580 g in T3. Calcite was dominant, with moderate (104) peak shifts, and morphologies were mainly spheroidal and sunflower-like. These findings indicate Zn was sequestered primarily through coprecipitation in calcite, with little contribution from discrete phases.

Chromium retention in carbonate systems appears to be governed more by redox behaviour than by direct structural substitution into calcite (Lai and McNeill, 2006; Wang et al., 2025). Under alkaline conditions, Cr(III) readily precipitates and can be partially incorporated into carbonate phases, but its long-term stability is strongly redox-sensitive.

Re-oxidation of Cr(III) to the more mobile Cr(VI) may occur in the presence of strong oxidants such as chlorine or manganese oxides, whereas dissolved oxygen promotes re-oxidation only slowly (Lai and McNeill, 2006). Unlike Pb and Zn, no systematic partitioning data exist for Cr substitution in calcite, suggesting that immobilisation pathways are primarily controlled by aqueous chemistry and redox environment rather than by lattice incorporation. Our experiments confirmed high removal efficiencies for chromium, consistently exceeding 99 per cent, although with slightly greater variability across treatments compared with Pb and Zn. Final pH values remained above 8.0 and residual ammonium concentrations exceeded 3,000 ppm, indicating only moderate inhibition of ureolysis and sustained alkalisation. Precipitate mass, however, declined sharply with increasing Cr concentration, from 1.773 g in T1 to 0.252 g in T3, suggesting that higher Cr loads suppressed carbonate precipitation efficiency. Morphological analysis revealed a systematic progression: at low concentrations (T1), carbonate aggregates exhibited well-developed crystalline habits; at intermediate concentrations (T2), spheroidal morphologies became dominant; and at the highest load (T3), poorly defined porous and lamellar aggregates prevailed. XRD confirmed calcite as the principal phase but showed the most pronounced shift of the (104) reflection among all metals tested, consistent with lattice distortions induced by Cr incorporation and/or organic interactions during crystallisation. The ranking of peak displacements (Cr > Li ≈ Ni > Zn > Pb > Cd > Control > Co) highlights the strong structural influence of Cr on the calcite lattice.

Taken together, these results suggest that in Ca-driven EICP systems, chromium immobilisation is highly efficient but mechanistically distinct from Pb and Zn. Retention depends less on structural substitution into calcite and more on the interplay between carbonate precipitation, system alkalisation and redox stability. The strong variability in precipitate mass and progressive morphological changes indicate that high chromium loads alter carbonate growth pathways, producing less ordered and more defective mineral assemblages while still maintaining overall removal efficiencies above 99 per cent.

The third group comprises arsenic, copper and lithium, which were less efficiently immobilised than Pb, Zn, Cr, Ni, Co and Cd, and displayed distinct retention pathways reflecting their divergent crystal–chemical behaviours.

Arsenic differs from divalent cations by occurring as oxyanions. Laboratory studies have shown stronger interactions of calcite with As(V) than with As(III), with preferential uptake via bidentate complexes and substitution of carbonate groups (Mendez et al., 2017). Mg-bearing calcite enhances this effect by increasing surface charge and roughness (Ladeira and Ciminelli, 2004). In situ AFM and XAS investigations confirm that As(V) can be incorporated during both growth and dissolution, whereas As(III) is less strongly retained and may be partly oxidised to As(V) in co-precipitated nanocalcite (Alexandratos et al., 2007; Román-Ross et al., 2006). In our experiments, As removal exceeded 95 per cent but remained lower than Pb, Zn and Cr. Final pH values remained above 8.0 and ammonium concentrations over 3,000 ppm indicated minimal inhibition of ureolysis. Precipitate masses were stable (1.62–1.70 g), with calcite as the main crystalline phase. Morphologically, aggregates were spheroidal with occasional

irregular textures, consistent with partial lattice incorporation and adsorption mechanisms.

Copper followed a different pathway, with immobilisation primarily through discrete carbonate phases rather than lattice substitution. Experimental work has shown that basic salts such as malachite or posnjakite form readily in carbonate-rich media (Zhizhaev and Merkulova, 2014), while mechanochemical activation with $CaCO_3$ yields basic copper carbonate alongside gypsum, enhancing immobilisation of other metals (Li et al., 2020). In our system, Cu removal exceeded 95 per cent, though ureolysis was partly inhibited, as evidenced by slightly reduced final pH (7.9–8.0) and lower ammonium accumulation relative to the control. Precipitate mass declined from 1.72 g in T1 to 0.398 g in T3. XRD confirmed calcite as the dominant phase but with additional reflections consistent with basic copper carbonates. Morphologically, aggregates showed irregular angular and plate-like textures distinct from the spheroidal and sunflower forms observed in other treatments.

Lithium showed the lowest immobilisation efficiencies among the tested elements, in agreement with its atypical crystal chemistry. Instead of simple substitution for Ca^{2+}, Li incorporates sectorally and epitaxially into calcite growth sectors where structural coincidence with zabuyelite (Li_2CO_3) allows mixed crystals (Pastero and Aquilano, 2008). Laboratory data indicate that its distribution coefficient increases with calcite growth rate but decreases with pH at constant rate, suggesting impurity trapping at rapidly growing surfaces and charge-balanced adsorption with bicarbonate (Okumura et al., 2011). In our experiments, Li removal efficiencies ranged from 85 to 92 per cent. Ureolysis was not significantly inhibited (pH above 8.0 and ammonium near 3,000 ppm), but precipitate mass decreased from 1.72 g in T1 to 0.312 g in T3. Morphologically, precipitates formed irregular porous aggregates with poorly defined boundaries. XRD confirmed calcite as the principal phase, with only subtle peak shifts, consistent with limited structural substitution.

Taken together, these results indicate that while As, Cu and Li were immobilised with reasonable efficiencies, their pathways differ fundamentally from those of the more strongly retained metals. Arsenic is stabilised mainly through adsorption and partial lattice incorporation, copper through the formation of discrete carbonate phases, and lithium by sectoral entrapment and minor substitution.

4.3 Mechanistic insights and analytical considerations

Organic moieties in the extract, including carboxylic, phenolic and phosphate groups, likely contributed to mineral modulation. Phosphorylated proteins or phospholipids may have formed complexes with Ca^{2+} or adsorbed to growth faces, altering morphology or even inhibiting crystallisation. These processes may explain suppression of typical carbonate phases in certain metal treatments, particularly under high organic load and moderate supersaturation.

Macromolecular adsorption can also influence kinetics, stabilising prenucleation clusters, delaying nucleation and reducing crystal size. Such interactions may favour amorphous over crystalline phases. The irregular morphologies observed in several samples, and the absence of XRD-detectable phases in some metals, are consistent with these kinetic effects.

Analytical limitations must also be acknowledged. SEM-EDS and FTIR confirm metal retention and organic associations but cannot fully resolve whether metals are incorporated into the calcite lattice, adsorbed at surfaces or present as nanocrystalline phases. Advanced techniques such as solid-state NMR, EXAFS or synchrotron microanalysis would be required to resolve these coordination environments in organically rich, multi-component systems.

4.4 Implications and future directions

The results demonstrate that crude soybean urease extract can support broad-spectrum removal of toxic metals through EICP, achieving immobilisation efficiencies comparable to or greater than those reported in other systems. The mineralogical and morphological evidence indicates a dual mechanism, combining incorporation into calcite with modulation by organic biomolecules. The distinctive flower-like structures suggest that plant-derived organics not only catalyse ureolysis but also influence crystallisation pathways.

Future studies should seek to quantify the molecular drivers of this modulation, identify functional groups responsible for templating and assess their stability across contrasting environmental conditions and for more than one metal. The use of higher-resolution analytical tools would allow incorporation pathways to be clarified and the long-term robustness of metal sequestration to be evaluated. Together, these insights strengthen the case for plant-derived EICP as a scalable and versatile approach for the remediation of metal-contaminated environments.

These findings provide the basis for the conclusions that follow, highlighting both the current strengths of the method and the opportunities for its further development.

5 Conclusions

Enzyme-induced carbonate precipitation (EICP) using a crude soybean urease extract immobilised a broad suite of ecotoxic metals (As, Cd, Co, Cr, Cu, Li, Ni, Pb, Zn) under controlled aqueous conditions. Across all systems, calcite formed consistently as the dominant phase, with element-specific carbonates detected where favoured (e.g., cerussite for Pb at ~2–4% and trace otavite for Cd). Performance grouped into clear tiers and an overall sequence (based on mean removal across T1–T3 over 72 h):

$$\mathrm{Pb} \approx \mathrm{Zn} \approx \mathrm{Cr} > \mathrm{Co} \geq \mathrm{Ni} > \mathrm{Cd} \geq \mathrm{Li} > \mathrm{As} \geq \mathrm{Cu}.$$

Here, “≈/≥” denote ties or near-ties where standard deviations overlap.

The most efficiently immobilised metals were lead, zinc and chromium, all achieving removal rates above 99 per cent and forming stable mineral phases. Nickel and cobalt also showed high efficiencies of 95 to 98 per cent, while cadmium and lithium performed moderately at around 89 to 93 per cent. Arsenic and copper, although still removed at levels above 70 per cent, showed clearer signs of urease inhibition. Cu^{2+} and As(III) showed the strongest urease inhibition (lower final pH and NH_4^+), whereas other metals had minimal impact on ureolysis. Crystallographic shifts of the calcite (104) reflection (largest for Cr) and distinctive spheroidal/"sunflower" textures indicate dual pathways—co-precipitation with limited lattice substitution plus organic modulation by biomolecules in the crude extract.

Operationally, an adaptive optimisation workflow (low-power juicing, single-step clarification, minimal reagents) reduced energy use, chemical inputs, and associated GHG burdens without compromising performance. While commercial $CaCl_2$ and urea were used for standardisation, both can be replaced by waste-derived sources (e.g., eggshell Ca, urine urea) to enable circular EICP. Ammonium management remains a key scale-up design requirement.

Overall, crude-extract EICP emerges as a scalable, lower-footprint route for metal immobilisation and carbon sequestration via stable carbonate phases. Priorities for deployment include (1) mixed-metal systems to map competition/synergy, (2) molecular-scale speciation (e.g., EXAFS/ssNMR) to resolve lattice vs. surface partitioning, and (3) process integration with waste-to-reagent supply chains and continuous reactors.

References

Alarifi SA, Mustafa A, Omarov K, Baig AR, Tariq Z, Mahmoud M. A Review of Enzyme-Induced Calcium Carbonate Precipitation Applicability in the Oil and Gas Industry. Front Bioeng Biotechnol. 2022 Jun 20;10:900881. doi: 10.3389/fbioe.2022.900881.

Almajed, A., Lateef, M. A., Moghal, A. A. B., & Lemboye, K. (2021). State-of-the-art review of the applicability and challenges of microbial-induced calcite precipitation (Micp) and enzyme-induced calcite precipitation (eicp) techniques for geotechnical and geoenvironmental applications. In *Crystals* (Vol. 11, Issue 4). MDPI AG. https://doi.org/10.3390/cryst11040370

Ahenkorah, I., Rahman, M. M., Karim, M. R., Beecham, S., & Saint, C. (2021). A Review of Enzyme Induced Carbonate Precipitation (EICP): The Role of Enzyme Kinetics. In *Sustainable Chemistry* (Vol. 2, Issue 1, pp. 92–114). Multidisciplinary Digital Publishing Institute (MDPI). https://doi.org/10.3390/suschem2010007

Ahenkorah, I., Rahman, M. M., Karim, M. R., & Teasdale, P. R. (n.d.). *Optimization of Enzyme Induced Carbonate Precipitation (EICP) as a Ground Improvement Technique*.

Almajed, A., Abbas, H., Arab, M., Alsabhan, A., Hamid, W., & Al-Salloum, Y. (2020). Enzyme-Induced Carbonate Precipitation (EICP)-Based methods for ecofriendly stabilization of different types of natural sands. *Journal of Cleaner Production*, *274*. https://doi.org/10.1016/j.jclepro.2020.122627

Almajed, A., Lateef, M. A., Moghal, A. A. B., & Lemboye, K. (2021). State-of-the-art review of the applicability and challenges of microbial-induced calcite precipitation (Micp) and enzyme-induced calcite precipitation (eicp) techniques for geotechnical and geoenvironmental applications. In *Crystals* (Vol. 11, Issue 4). MDPI AG. https://doi.org/10.3390/cryst11040370

Alotaibi, E., Arab, M. G., Abdallah, M., Nassif, N., & Omar, M. (2022). Life cycle assessment of biocemented sands using enzyme induced carbonate precipitation (EICP) for soil stabilization applications. *Scientific Reports*, *12*(1). https://doi.org/10.1038/s41598-022-09723-7

Arab, M. G., Alsodi, R., Almajed, A., Yasuhara, H., Zeiada, W., & Shahin, M. A. (2021). State-of-the-art review of enzyme-induced calcite precipitation (Eicp) for ground improvement: Applications and prospects. In *Geosciences (Switzerland)* (Vol. 11, Issue 12). MDPI. https://doi.org/10.3390/geosciences11120492

Chen, Y., Liu, Y., Gao, Y., Zhou, Y., Liu, B., Wang, L., Hang, L., & Zhang, S. (2025). Comparison of Crude Soybean Urease- and Pure Urease-Induced Carbonate Precipitation on Wind-Induced Erosion Resistance of Desert Sand. *Sustainability (Switzerland)*, *17*(7). https://doi.org/10.3390/su17072968

Crane, L., Ray, H., Hamdan, N., & Boyer, T. H. (2022). Enzyme-induced carbonate precipitation utilizing fresh urine and calcium-rich zeolites. *Journal of Environmental Chemical Engineering*, *10*(2). https://doi.org/10.1016/j.jece.2022.107238

Cui, M. J., Lai, H. J., Hoang, T., & Chu, J. (2021). One-phase-low-pH enzyme induced carbonate precipitation (EICP) method for soil improvement. *Acta Geotechnica*, *16*(2), 481–489. https://doi.org/10.1007/s11440-020-01043-2

Gao, Y., He, J., Tang, X., & Chu, J. (2019). Calcium carbonate precipitation catalyzed by soybean urease as an improvement method for fine-grained soil. *Soils and Foundations*, *59*(5), 1631–1637. https://doi.org/10.1016/j.sandf.2019.03.014

Ghasemi, H., Hatam-Lee, S. M., Khodadadi Tirkolaei, H., & Yazdani, H. (2022). Biocementation of soils of different surface chemistries via enzyme induced carbonate precipitation (EICP): An integrated laboratory and molecular dynamics study. *Biophysical Chemistry*, *284*. https://doi.org/10.1016/j.bpc.2022.106793

Gonzalez, V., Vignati, D. A. L., Leyval, C., Giamberini, L., & Dominik, J. (2017). Chromium behaviour in aquatic environments: A review. *Environmental Reviews, 25*(2), 199–213. https://doi.org/10.1139/er-2016-0012

Hu, W., Cheng, W. C., Wen, S., & Yuan, K. (2021). Revealing the Enhancement and Degradation Mechanisms Affecting the Performance of Carbonate Precipitation in EICP Process. *Frontiers in Bioengineering and Biotechnology*, *9*. https://doi.org/10.3389/fbioe.2021.750258

Krajewska, B. (2018). Urease-aided calcium carbonate mineralization for engineering applications: A review. In *Journal of Advanced Research* (Vol. 13, pp. 59–67). Elsevier B.V. https://doi.org/10.1016/j.jare.2017.10.009

Kim, J. J., Lee, S. S., Fenter, P., Myneni, S. C. B., Nikitin, V., & Peters, C. A. (2023). Carbonate coprecipitation for Cd and Zn treatment and evaluation of heavy metal stability under acidic conditions. *Environmental Science & Technology, 57*(8), 3104–3113. https://doi.org/10.1021/acs.est.2c07678

Lai, H. and L.S. McNeill, "Chromium Redox Chemistry in Drinking Water Systems," Journal of Environmental Engineering, 132(8), 842-851, August 2006. https://doi.org/10.1061/(ASCE)0733-9372(2006)132:8(842)

Li, W., Zhang, Y., & Achal, V. (2022). Mechanisms of cadmium retention on enzyme-induced carbonate precipitation (EICP) of Ca/Mg: Nucleation, chemisorption, and co-precipitation. *Journal of Environmental Chemical Engineering*, *10*(3). https://doi.org/10.1016/j.jece.2022.107507

Martin, K. K., Asce, S. M., Khodadadi, ; T Hamed, Chester, M., Kavazanjian, E., & Ge, D. (n.d.-a). *Hotspot Life Cycle Assessment for Environmental Impacts of EICP for Ground Improvement*.

Martin, K. K., Asce, S. M., Khodadadi, ; T Hamed, Chester, M., Kavazanjian, E., & Ge, D. (n.d.-b). *Hotspot Life Cycle Assessment for Environmental Impacts of EICP for Ground Improvement*.

Meng, H., Shu, S., Gao, Y., Yan, B., & He, J. (2021). Multiple-phase enzyme-induced carbonate precipitation (EICP) method for soil improvement. *Engineering Geology*, *294*. https://doi.org/10.1016/j.enggeo.2021.106374

Moghal, A. A. B., Lateef, M. A., Mohammed, S. A. S., Ahmad, M., Usman, A. R. A., & Almajed, A. (2020). Heavy metal immobilization studies and enhancement in geotechnical properties of cohesive soils by eicp technique. *Applied Sciences (Switzerland)*, *10*(21), 1–21. https://doi.org/10.3390/app10217568

Nawarathna, T. H. K., Nakashima, K., & Kawasaki, S. (2019). Chitosan enhances calcium carbonate precipitation and solidification mediated by bacteria. *International Journal of Biological Macromolecules*, *133*, 867–874. https://doi.org/10.1016/j.ijbiomac.2019.04.172

Oktafiani, P. G., Putra, H., Erizal, & Yanto, D. H. Y. (2022). Application of technical grade reagent in soybean-crude urease calcite precipitation (SCU-CP) method for soil improvement technique. *Physics and Chemistry of the Earth*, *128*. https://doi.org/10.1016/j.pce.2022.103292

Ossai, R., Asce, S. M., Rivera, ; Lucas, Bandini, P., & Asce, M. (n.d.-a). *Experimental Study to Determine an EICP Application Method Feasible for Field Treatment for Soil Erosion Control*.

Ossai, R., Asce, S. M., Rivera, ; Lucas, Bandini, P., & Asce, M. (n.d.-b). *Experimental Study to Determine an EICP Application Method Feasible for Field Treatment for Soil Erosion Control*.

Patil, M., Dalal, P. H., Shreedhar, S., Dave, T. N., & Iyer, K. K. R. (2021). Biostabilization techniques and applications in Civil Engineering: State-of-the-Art. In *Construction and Building Materials* (Vol. 309). Elsevier Ltd. https://doi.org/10.1016/j.conbuildmat.2021.125098

Pratama, G. B. S., Yasuhara, H., Kinoshita, N., & Putra, H. (2021). Application of soybean powder as urease enzyme replacement on EICP method for soil improvement technique. *IOP Conference Series: Earth and Environmental Science*, *622*(1). https://doi.org/10.1088/1755-1315/622/1/012035

Putra, H., Yasuhara, H., Kinoshita, N., Neupane, D., & Lu, C. W. (2016). Effect of magnesium as substitute material in enzyme-mediated calcite precipitation for soil-improvement technique. *Frontiers in Bioengineering and Biotechnology*, *4*(MAY). https://doi.org/10.3389/fbioe.2016.00037

Rosa, D., Verdirame, L., Bavasso, I., Bracciale, M. P., & di Palma, L. (2023). Soil Biocementation via Enzyme Induced Carbonate Precipitation (EICP) Method Employing Soybeans as a Source of Cheap Enzyme. *Chemical Engineering Transactions*, *99*, 157–162. https://doi.org/10.3303/CET2399027

Saif, A., Cuccurullo, A., Gallipoli, D., Perlot, C., & Bruno, A. W. (2022). Advances in Enzyme Induced Carbonate Precipitation and Application to Soil Improvement: A Review. In *Materials* (Vol. 15, Issue 3). MDPI. https://doi.org/10.3390/ma15030950

Wang, H., Sun, X., Miao, L., Cao, Z., & Guo, X. (2023). Garlic extract addition for soil improvement at various temperatures using enzyme-induced carbonate precipitation (EICP) method. *Journal of Rock Mechanics and Geotechnical Engineering*, *15*(12), 3230–3243. https://doi.org/10.1016/j.jrmge.2023.03.018

Wang, L., Cheng, W. C., Xue, Z. F., Zhang, B., & Lv, X. J. (2023). Immobilizing of lead and copper using chitosan-assisted enzyme-induced carbonate precipitation. *Environmental Pollution*, *319*. https://doi.org/10.1016/j.envpol.2022.120947

Wang, Y., Wang, Z., Chen, Y., Cao, T., Yu, X., & Rui, P. (2023). Experimental study on bio-treatment effect of the dredged Yellow River silt based on soybean urease induced calcium carbonate precipitation. *Journal of Building Engineering*, *75*. https://doi.org/10.1016/j.jobe.2023.106943

Xu, X., Guo, H., Li, M., & Deng, X. (2021). Bio-cementation improvement via CaCO3 cementation pattern and crystal polymorph: A review. *Construction and Building Materials*, *297*. https://doi.org/10.1016/j.conbuildmat.2021.123478

Yuan, H., Liu, K., Zhang, C., & Zhao, Z. (n.d.). *Mechanical properties of Na-montmorillonite-modified EICP-treated silty sand*. https://doi.org/10.1007/s11356-021-16442-5/Published

Zhang, Q., Ye, W., Liu, Z., Wang, Q., & Chen, Y. (2023). Influence of injection methods on calcareous sand cementation by EICP technique. *Construction and Building Materials*, *363*. https://doi.org/10.1016/j.conbuildmat.2022.129724